Available online at www.sciencedirect.com
ScienceDirect
Fuel 87 (2008) 319–334
FUEL
www.fuelfirst.com

A numerical and experimental study of counterflow syngas flames at different pressures

S. Som, A.I. Ramírez, J. Hagerdorn, A. Saveliev, S.K. Aggarwal *

Department of Mechanical and Industrial Engineering, University of Illinois, 842 West Taylor Street, Chicago, IL 60607-7022, USA

Received 5 October 2006; received in revised form 2 April 2007; accepted 3 May 2007
Available online 11 June 2007

Abstract

Synthesis gas or "Syngas" is being recognized as a viable energy source worldwide, particularly for stationary power generation due to its wide availability as a product of bio and fossil fuel gasification. There are, however, gaps in the fundamental understanding of syngas combustion and emissions characteristics, especially at elevated pressures that are relevant to practical combustors. This paper presents a numerical and experimental investigation of the combustion and NO_x characteristics of syngas fuel with varying composition, pressure and strain rate. Experiments were performed at atmospheric conditions, while the simulations considered different pressures. Both experiments and simulations indicate that stable non-premixed and partially premixed counterflow flames (PPFs) can be established for a wide range of syngas compositions and strain rates. Three chemical kinetic models, GRI 3.0, Davis et al., and Mueller et al. are examined. The Davis et al. mechanism is found to agree best with the experimental data, and hence used to simulate the PPF structure at different pressure and fuel composition. For the pressure range investigated, results indicate a typical double flame structure with a rich premixed reaction zone (RPZ) on the fuel side and a non-premixed reaction zone (NPZ) on the oxidizer side, with RPZ characterized by H_2 oxidation, and NPZ by both H_2 and CO oxidation. While thermal NO is found to be the dominant route for NO production, a reburn route, which consumes NO through $NO + O + M \rightarrow NO_2 + M$ and $H + NO + M \rightarrow HNO + M$ reactions, becomes increasingly important at high pressures. The amount of NO formed in syngas PPFs first increases rapidly with pressure, but then levels off at higher pressures. At a given pressure, the peak NO mole fraction exhibits a non-monotonic variation with syngas composition, first decreasing to a minimum value, and then increasing as the amount of CO in syngas is increased. This implies the existence of an optimum syngas composition that yields the lowest amount of NO production in syngas PPFs, and can be attributed to the combined effects of thermal and reburn mechanisms.
© 2007 Elsevier Ltd. All rights reserved.

Keywords: High pressure; Syngas flames; Partially premixed; NO_x emissions

1. Introduction

In the wake of increasingly strict emission laws imposed by the US Environmental Protection Agency and limited fossil fuel availability, there is a worldwide interest in the utilization of alternative and environmentally benign energy sources. Hydrogen represents potentially an unlimited source of energy since it can be produced through electrolysis of water as well as partial oxidation and reforming of natural hydrocarbons. However, due to its high flammability and low volumetric energy density, many critical issues pertaining to hydrogen safety and storage still need to be addressed. Consequently, blending hydrogen with other hydrocarbon fuels is an attractive option. In this context, synthesis gas (mainly a mixture of CO/H_2) or "syngas" is being recognized as a viable energy source worldwide, especially for stationary power generation. Syngas is formed through gasification processes, and can be produced from virtually any fossil fuel, including coal, biomass, organic waste, and refinery residual [1,2]. It is particularly attractive for stationary power generation, since it allows for a wide flexibility in fossil fuel sources,

* Corresponding author. Tel.: +1 312 996 2235; fax: +1 312 413 0441.
E-mail address: ska@uic.edu (S.K. Aggarwal).

0016-2361/$ - see front matter © 2007 Elsevier Ltd. All rights reserved.
doi:10.1016/j.fuel.2007.05.023

and most of the harmful contaminants and pollutants can be removed in the post-gasification process prior to combustion. Moreover, improvements in gas turbine efficiency and reliability have made syngas a viable fuel for electric power generation using Integrated Gasification Combined Cycle (IGCC) systems [3]. However, environmental feasibility of syngas usage needs to be fully established, in particular, NO_x emissions from syngas combustion must comply with the current and future emission regulations. Recent Department of Energy (DOE) initiatives aim to reduce NO_x emissions from syngas combustion systems to less than 3 PPM, well below the current US regulations [3]. Hence, fundamental research focusing on syngas combustion and emissions forms a major motivation for the current study.

Several studies have been reported on the combustion and emission characteristics of non-premixed syngas–air mixtures. Drake and Blint [4] numerically investigated the effect of stretch on thermal NO in laminar, counterflow $CO/H_2/N_2$ diffusion flames, and observed that NO concentration decreases dramatically as the flame stretch is increased. Chung and Williams [5] analyzed the structure and extinction of a $CO/H_2/N_2$ diffusion flame using an asymptotic approach with the kinetic scheme systematically reduced to the two-step mechanism $CO + H_2O \rightleftarrows CO_2 + H_2$, $2H_2 + O_2 \rightleftarrows 2H_2O$, the water–gas shift, and hydrogen oxidation. It was shown that a three-step mechanism is needed to obtain a reasonably accurate description of the water–gas freezing. Fotache et al. [6] examined experimentally and numerically the ignition characteristics of a $CO/H_2/N_2$ mixture using heated air in a counterflow configuration. The experiments confirmed the numerical modeling observation of the existence of three ignition regimes as a function of the hydrogen concentration. Rumminger and Linteris [7] reported an experimental and numerical investigation on the burning velocity of premixed $CO/H_2/O_2/N_2$ flames with the objective of assessing the fire inhibition characteristics of iron pentacarbonyl. Jurgen et al. [8] modeled and measured a 16KW turbulent non-adiabatic syngas diffusion flame in a cooled cylindrical combustion chamber. Their calculated CO, CO_2, O_2, and NO concentrations compared well with measurements. Recently, Giles et al. [9] studied the NO_x emission characteristics of counterflow syngas diffusion flames with air-stream dilutions at $p = 1$ atm. The results indicated that addition of methane in syngas decreases the peak flame temperature but increases prompt NO significantly.

Combustion and emission characteristics of premixed syngas–air mixtures have also been studied. Charlston-Goch et al. [10] reported measurement and computation of NO concentrations in premixed $CO/H_2/CH_4$/air flames for a range of equivalence ratios, fuel compositions, and strain rates at high pressures ($p \leqslant 11.9$ atm). GRI 2.11 mechanism was observed to uniformly overpredict NO concentrations, and failed to predict key experimental trends. Natarajan et al. [11] also reported measurement and computation of laminar flame speeds of $H_2/CO/CO_2$ mixtures over a range of fuel compositions, lean equivalence ratios, and reactant preheat temperatures. Alavandi and Agrawal [12] investigated experimentally the lean premixed combustion of $CO/H_2/CH_4$/air mixture, and observed that at a given flame temperature, the presence of CH_4 in a CO–H_2 mixture increases CO and NO_x emissions. The effects of syngas addition on the laminar flame speeds and flammability limits of *n*-butane and *iso*-butane flames have been reported by Sung et al. [13]. Huang et al. [14] computed the laminar flame speeds of primary reference fuels and syngas mixtures and observed that the flame speed of hydrocarbon/air mixtures increases with a small addition of syngas, and that of syngas/air mixtures decrease dramatically with a small addition of hydrocarbon fuel. Saxena and Williams [15] developed a relatively small mechanism for CO/H_2 combustion. The mechanism was tested against the available data and some rate parameters were modified to obtain a new reduced mechanism. Recently, Sun et al. [16] measured laminar flame speeds for CO/H_2/air ($p \leqslant 2$ atm) and CO/H_2/helium ($p \leqslant 40$ atm) mixtures at different equivalence ratios by the constant pressure spherical flame technique. A kinetic model was also developed which accurately predicted the measured flame speeds at different pressures, and also exhibited good agreement against other validation targets.

Considerable efforts have been expended in studying the combustion characteristics of the carbon monoxide–hydrogen system, motivated primarily by its essential role in the hierarchical structure of oxidation models of hydrocarbon fuels [17]. Allen et al. [18] studied the oxidation chemistry of $CO/H_2O/N_2$ mixtures by performing flow reactor experiments over the pressure range of 3–15 atm and temperature range of 950—1123 K. The developed chemical kinetic mechanism was validated against CO, CO_2, N_2O, NO, O_2, H_2O, and temperature profiles. The ongoing quest to improve H_2–CO chemical-kinetic models has seen the evolution of two detailed chemistry models by Davis et al. [19] and Mueller et al. [20]. The H_2 chemistry from the Mueller et al. mechanism was modified by Li et al. [21]. The Davis et al. model incorporates the recent thermodynamic, kinetic, and species transport updates relevant to high-temperature H_2–CO combustion. The model was validated against reliable H_2–CO combustion data (shock-tube ignition delays, laminar flame speeds and extinction strain rates). Mueller et al. [20] performed flow reactor experiments over a wide range of pressure and temperature to study H_2/O_2 and $O_2/H_2O/O_2$ kinetics in the presence of trace amounts of NO and NO_2. Experimentally measured species and temperature profiles were used to guide the development of this mechanism. Model predictions were in good agreement with the experimental data over the entire range of conditions explored. Hence, the H_2–CO oxidation chemistry which forms an integral part of other hydrocarbon reaction chemistry is relatively well understood. Both the above mechanisms will be used for the current investigation.

Our literature review indicates that emission and extinction characteristics of non-premixed syngas flames have

been studied in some detail under atmospheric conditions. Laminar flame speeds have been measured at different pressures ($p \leqslant 11.9$ atm). Ignition characteristic of syngas mixtures have also been investigated. However, combustion in many important applications like, gas turbine combustors, occurs at high pressures and involves partially premixed flames (PPFs). Partially premixed flame in counterflow configuration is established using two opposing jets, one containing fuel-rich mixture and other containing air. A PPF typically contains two or more reaction zones that are synergistically coupled. For example, in a methane–air PPF containing two reaction zones, the fuel is consumed in the rich premixed zone producing the ''intermediate fuels'', such as CO and H_2, which are then transported to and consumed in the non-premixed zone. The latter zone in turn provides heat and radical species to the rich premixed zone. As a result of these interactions, PPFs can exploit the advantages of both non-premixed and premixed flames with regards to safety and flame stability, and also provide higher energy output with lower emissions [22]. While PPFs have been extensively investigated in recent years [23,24], none of the previous studies have considered such flames burning syngas mixtures. Moreover, the effect of pressure on the structure and emission characteristics of such flames has not been characterized. Consequently, there are important gaps in our basic understanding of this important class of flames burning syngas–air mixtures.

2. Objectives

In this paper, we report a numerical and experimental study of non-premixed and partially premixed syngas flames at different pressures. The syngas fuel is assumed to contain H_2 and CO species. The experimental investigation is performed under atmospheric conditions to identify parametric regime, in terms of syngas composition and strain rate, for which syngas flames can be established in a counterflow configuration. Note that this represents the first experimental study of partially premixed syngas flames in a counterflow configuration. In order to perform numerical simulations of syngas flames at different pressures, a detailed chemical kinetic model for syngas fuel oxidation is validated using the available experimental data on laminar flame speeds as well as our measurements of non-premixed and partially premixed flames. This model is combined with a detailed NO_x chemistry model, and then employed to examine the structure and NO_x emission characteristics of syngas partially premixed flames (PPFs) at high pressures. This is motivated from the consideration that syngas combustion in practical systems generally occurs at elevated pressures, and the syngas composition can vary widely depending upon the fuel source, gasification process and post gasification treatment. Therefore, it is important to examine the effect of pressure and syngas composition on the structure and NO_x characteristics of syngas flames. The present study of syngas PPFs is also motivated by the consideration of examining the differences and similarities between the structures and NO_x emission characteristics of syngas and hydrocarbon (such as methane) PPFs.

The counterflow partially premixed syngas flames are simulated using the following fuel mixture volumetric composition: 98%CO–2%H_2 (Flame E), 95%CO–5%H_2 (Flame B), 85%CO–15%H_2 (Flame G), 75%CO–25%H_2 (Flame C), 50%CO–50%H_2 (Flame A), 25%CO–75%H_2 (Flame D) and 10%CO–90%H_2 (Flame F). Two representative mixtures with 50%CO–50%H_2 (Flame A) and 95%CO–5%H_2 (Flame B) were selected for more extensive analysis. 50%CO–50%H_2 (Flame A) was chosen based on fuel composition data from multiple power generation plants worldwide. 95%CO–5%H_2 (Flame B) was chosen as the burning velocity for this mixture was identified to be most sensitive to CO + OH reaction [25].

3. Experimental setup

A schematic of the experimental setup used to establish syngas/air counterflow flames is presented in Fig. 1. A premixing chamber was used to generate a syngas mixture of carbon monoxide and hydrogen fuel. For non-premixed flames, the syngas fuel was introduced from the bottom nozzle, and air from the top nozzle. For partially premixed flames, a premixed mixture of syngas fuel and air at a specified rich equivalence ratio (ϕ) was introduced from the fuel nozzle, and air from the other nozzle. A nitrogen curtain was established through an annular duct surrounding the fuel jet in order to isolate the flames from ambient disturbances. This nitrogen and combustion products were vented and cooled through another annular duct around the oxidizer nozzle. The diameter of each nozzle was 27.4 mm, and the separation distance (L) between them was 12.7 mm. Strong suction was used to drain the excess fuel. The whole setup was enclosed in a sealed case to avoid the escape of CO into the laboratory. The velocities of the two streams define the global strain rate as $a_s = (2|v_o|/L) \cdot \{1 + |v_f|\sqrt{\rho_f}/|v_o|\sqrt{\rho_o}\}$ [26]. Here ρ represents density, v gas velocity, and the subscripts o and f refer to oxidizer and fuel nozzles, respectively. Table 1 presents the fuel and oxidizer velocities at different strain rates for various fuel mixture compositions used in the current investigation. It should be noted that for all results involving experimental studies, velocity of fuel and oxidizer streams were kept constant, i.e., $v_f = v_o$. However, for studies involving simulations only, the fuel and oxidizer stream momentum was balanced, i.e., $\rho_f v_f^2 = \rho_o v_o^2$. Temperature profiles of various flames were measured using a Pt–Pt 13% Rh thermocouple with a spherical bead diameter of 0.25 mm and wire diameter of 0.13 mm. The measured values were corrected for radiation heat losses from the bead, assuming a constant emissivity of 0.2 and a Nusselt number of 2.0 [27].

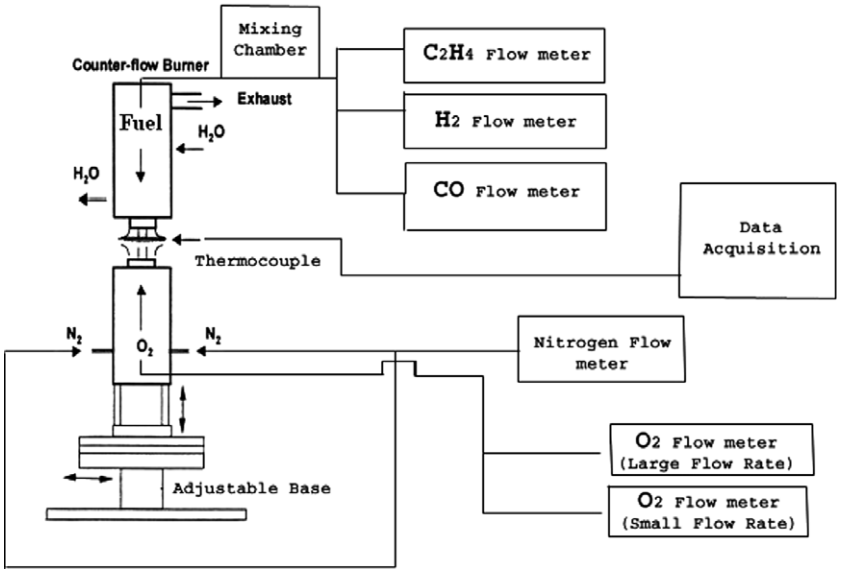

Fig. 1. Schematic diagram of the experimental setup.

Table 1
Strain rates and fuel and oxidizer velocities for different syngas mixtures used in the current study

Strain rate (s^{-1})	PPF (ϕ)/NPF	Fuel composition [CO:H_2]	Numerical	Experiments	V_o (cm/s)	V_f (cm/s)
35	NPF	50:50	X	X	13.84	13.84
35	NPF	97:3		X	12.18	12.18
35	NPF	90:10		X	12.37	12.37
35	NPF	100:0		X	12.10	12.10
15	NPF	50:50		X	5.18	5.18
65	NPF	50:50		X	22.47	22.47
115	NPF	50:50		X	39.75	39.75
143	NPF	50:50		X	49.43	49.43
35	PPF ($\phi = 6$)	50:50 (Flame A)	X	X	13.32	13.32
35	PPF ($\phi = 16$)	50:50 (Flame A)	X	X	14.27	14.27
50	PPF ($\phi = 6$)	50:50 (Flame A)	X	X	19.03	19.03
50	PPF ($\phi = 14$)	50:50 (Flame A)	X	X	20.23	20.23
100	PPF ($\phi = 6$)	98:2 (Flame E)	X		31.75	33.27
100	PPF ($\phi = 6$)	95:5 (Flame B)	X		31.75	31.94
100	PPF ($\phi = 6$)	85:15 (Flame G)	X		31.75	33.04
100	PPF ($\phi = 6$)	75:25 (Flame C)	X		31.75	34.27
100	PPF ($\phi = 6$)	50:50 (Flame A)	X		31.75	38.07
100	PPF ($\phi = 6$)	25:75 (Flame D)	X		31.75	43.49
100	PPF ($\phi = 6$)	10:90 (Flame F)	X		31.75	48.12

4. Physical and numerical model

The counterflow flame configuration employed in the present investigation has been discussed in our previous studies [9,22,23,28]. Simulations of syngas/air premixed flames at different equivalence ratios and pressures are performed using the PREMIX [29] code in the CHEMKIN [30] package. Simulations of counterflow syngas/air PPFs at a given equivalence ratio ($\phi = 6.0$), strain rate ($a_s = 100\ s^{-1}$), and varying pressures (p) are performed using the OPPDIF [31] code in the CHEMKIN [30] package. The effect of radiation is included by using an optically thin radiation model. The inclusion of radiation reduced the predicted flame temperature by 30 K for a low strain rate flame ($35\ s^{-1}$), and by 5 K for a relatively high strain rate flame ($100\ s^{-1}$). Moreover, the effect of radiation decreased with increase in pressure. The fuel and air stream temperatures were fixed at 300 K. The equivalence ratio was fixed to 6 to ensure that the PPFs simulated are beyond the rich flammability limit of freely propagating syngas flames. The grid independence of the results was achieved by controlling the values of the GRAD, CURV parameters and using adaptive re-gridding in order to resolve the structures of both the premixed and non-premixed reaction zones. This required the number of grid points to be 250 for the base case at 1 atm. At high pressures the number of grid points required to ensure grid independence increased to 900.

Three chemical kinetic models considered in the present study were the Davis et al. [19], Mueller et al. [20] and GRI

3.0 [32] mechanisms. The Davis et al. mechanism contains 14 species and 38 reactions, while the Mueller et al. mechanism contains 13 species and 25 reactions, and the GRI 3.0 mechanism including the NO_x chemistry model contains 53 species and 325 reactions. As discussed in a later section, the Davis et al. mechanism performed the best in terms of reproducing the experimental data. Consequently, this mechanism was employed for the detailed simulations of syngas flames under different conditions. In order to examine the NO_x emission characteristics, the NO_x chemistry from GRI 3.0 was incorporated into the Davis et al. mechanism, as this NO_x chemistry model has been previously validated against measurements at different pressures [24,28]. The modified Davis et al. mechanism (with NO_x chemistry) contains 38 species and 144 reactions. A few hundred elementary gas phase reactions are involved in the formation of NO_x, which can be formed or destroyed by at least five separate reaction processes [33]. They are classified as: thermal, prompt, N_2O, NNH, and reburn routes. In order to identify the relative importance of each route for NO formation, we have suppressed the reactions responsible for NO formation by the other routes [34].

5. Results and discussion

5.1. Validation

Fig. 2 plots the measured and predicted temperature profiles for counterflow non-premixed syngas/air flames established at $p = 1$ atm and $a_s = 35 s^{-1}$ for 50%H_2–50%CO mixture. The numerical results include the effect of radiation; experimental results are also radiation corrected. The peak values predicted by GRI 3.0 and Davis et al. mechanisms are in close agreement with the data; however, the peaks are shifted by ~0.18 cm. This is due to the strong suction employed to drain out the excess fuel [27]. Mueller et al. mechanism underpredicts the temperature peak and its location is also different from those predicted by the other two mechanisms. Therefore, both GRI 3.0 and Davis et al. mechanisms predict the temperature profile fairly accurately under atmospheric conditions.

Measurements of high-pressure syngas–air PPFs are yet to be reported, hence, it is difficult to select a reliable mechanism for the present investigation. However, laminar flame speed data for premixed syngas–air mixtures at $p = 1$ atm for different syngas composition has been reported by McLean et al. [25]. This data are used for further validation of the three reaction mechanisms mentioned earlier.

Fig. 3a presents the variation of measured and predicted laminar burning velocities for two freely propagating syngas–air flames, namely Flame A and Flame B. The computational model included thermal diffusion and multicomponent transport. The effect of thermal radiation was

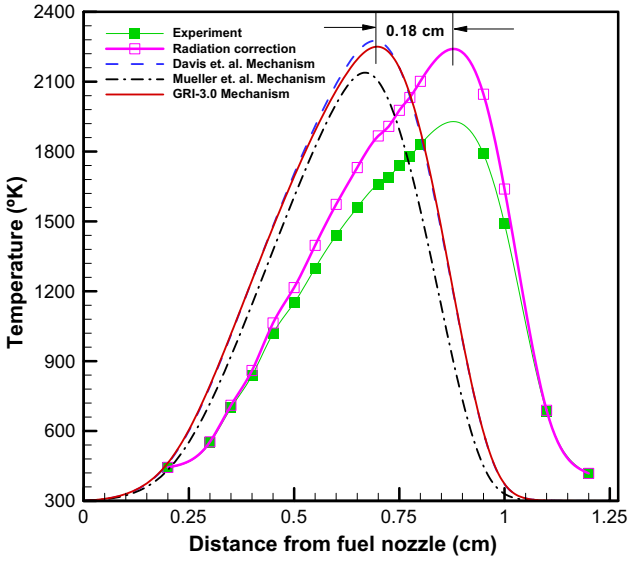

Fig. 2. Measured and predicted temperatures versus distance from the fuel nozzle for a counterflow non-premixed syngas/air flame established at $a_s = 35\ s^{-1}$.

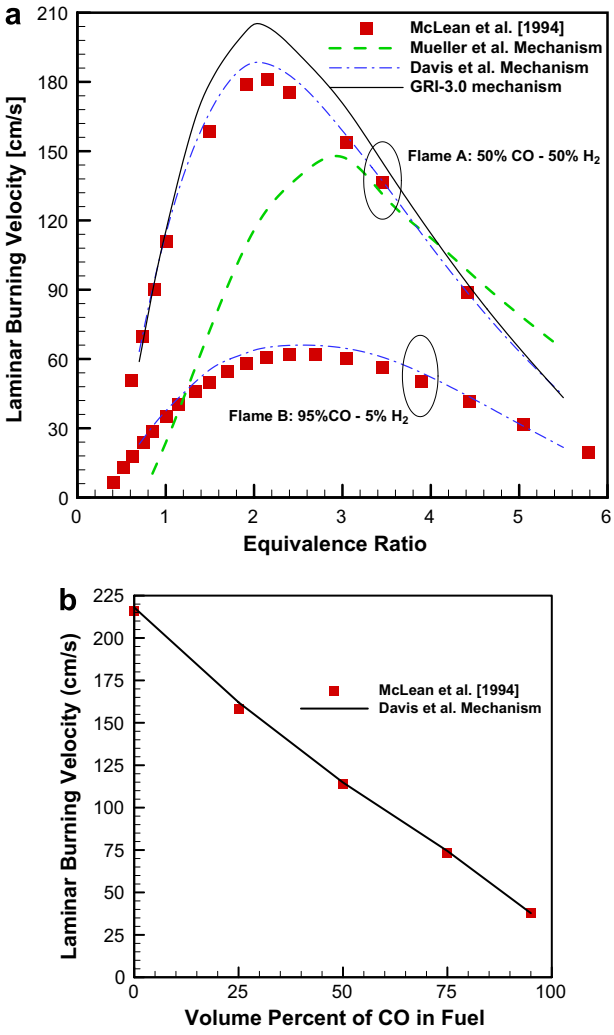

Fig. 3. Comparison of measured and predicted laminar burning velocities for Flames A and B. Variation of laminar burning velocity with equivalence ratio (a) and with volume percent of CO in syngas fuel at fixed $\phi = 2.0$ (b).

also considered using an optically thin radiation model. For Flame A, the Davis et al. mechanism predicts the flame speeds most accurately except for the peak values, which it overpredicts slightly. The GRI 3.0 mechanism also does a fair job except near the peak where it tends to overpredict significantly. The Mueller et al. mechanism underpredicts the flame speed for $\phi < 4.0$, but then overpredicts for higher ϕ values. Since the Davis et al. mechanism showed the best agreement with measurements for Flame A, it was used to compute laminar burning velocities for flame B. As indicated in Fig. 3a, the agreement with experimental values is again excellent. The rich and lean flammability limits predicted by all the three mechanisms are $\phi \approx 0.7$ and $\phi \approx 5.5$, respectively, for both the flames considered. The laminar burning velocity peaks at $\phi = 2.0$ for flame A, and at $\phi = 2.5$ for flame B. Fig. 3b presents the laminar burning velocity versus the volume percent of CO in syngas fuel for a fixed $\phi = 2$. The agreement between simulations using Davis et al. mechanism and experimental data are again excellent. The laminar burning velocity decreases with CO addition which is expected.

Since Davis et al. mechanism does the best job in predicting the laminar flame speeds for a wide range of conditions, and also shows fairly good agreement with the measured temperature profile for a non-premixed syngas flame; it is used further in this work to study the flame structure and NO_x emission characteristics at elevated pressures. Having identified a reliable chemical kinetic model for syngas oxidation, we now present experimentally obtained flame images as well as simulation results in order to identify the range of parameters, i.e., syngas composition and strain rate, for which syngas flames can be established in a counterflow configuration.

5.2. Stability analysis of syngas non-premixed mixtures

The stability analysis here refers to identifying parametric range, in terms of syngas composition and strain rate, for which stable, nearly one-dimensional syngas flames can be established under atmospheric conditions. The experimental images shown in Fig. 4 were taken using digital camera with constant exposure time. For all mixture compositions, an intense blue flame was observed. Blue light emissions from hydrocarbon flames are usually attributed to the presence of CH and C_2 excited bands [35]. In syngas flames (with no hydrocarbon addition) these species are expected to be absent in the flame (predicted numerically also). The intense blue color of carbon monoxide flames is due to CO_2^* continuum formed as CO reacts with O to form excited CO_2^* [35]. The strong CO_2 continuum extending over the spectral range from 350 to 450 nm was observed both in premixed and diffusion CO flames. The intensity of continuum is proportional to concentration of CO and atomic oxygen, but also a function of pressure and the nature of any diluent gas. The latter is usually attributed to the quenching of excited CO_2 molecules by the third body. In turn, the quenching rate strongly depends on the nature of this third body [35]. Several authors independently confirmed that hydrogen and moisture addition greatly affects the strength of the blue CO-emission [35]. The present experimental studies confirmed this trend as can be clearly observed from the increase of the blue light emissions with reduction of hydrogen content (Fig. 4). There is no soot formation for these flames which is in agreement with previous results.

Stable flames were observed for the range of H_2 concentrations (50% to 0%). With decreasing H_2 concentration

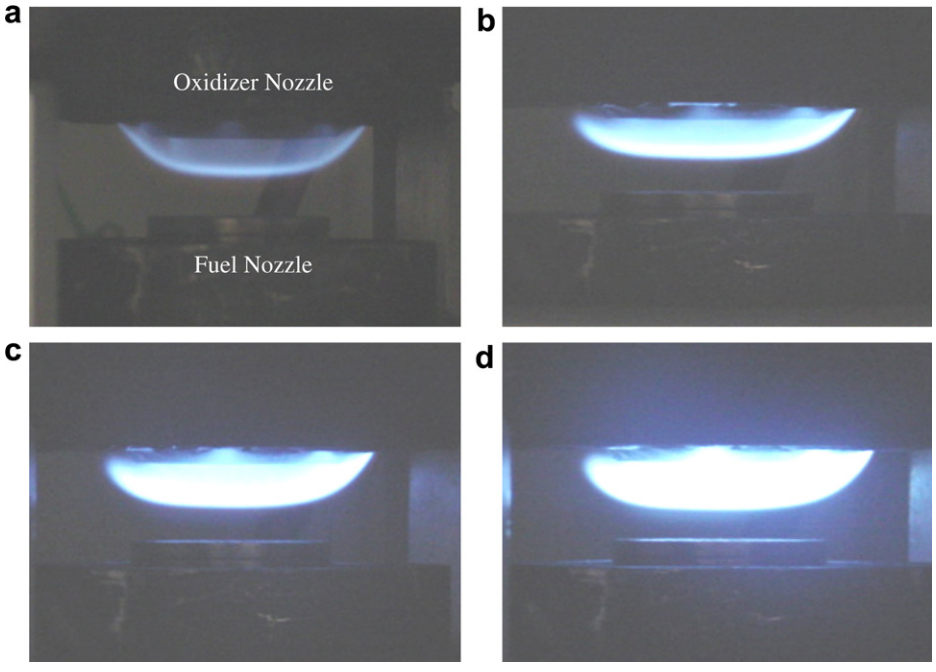

Fig. 4. Images of syngas/air non-premixed flames established at $p = 1$ atm, $a_s = 35\ s^{-1}$ for 50%H_2–50%CO (a), 10%H_2–90%CO (b), 3%H_2–97%CO (c) and 0%H_2–100%CO (d).

radical species like OH ($OH + CO \rightarrow CO_2 + H$ which is the main exothermic reaction) diminish, making the flame weaker. Hence, it is expected that there would be a critical H_2 concentration for burning with air below which there would be no flame. Thus, the existence of a flame with no H_2 presence was surprising. To understand this more clearly, simulations were run for different H_2 concentrations at the given strain rate and pressure. It was observed that 0.5% H_2 was needed to establish a flame. The chemical purity CO (BOC, Inc.) was used in the experiments. The overall CO content exceeded 99.5% with additional possible impurities such as N_2 (up to 0.3%), CO_2 (up to 0.15%), H_2O (up to 200 ppm), and O_2 (up to 50 ppm). Hence, it may be concluded that the 0%H_2–100%CO flame is established due to the impurities in the CO cylinder. The 0% H_2flame was also observed to be brighter than the other flames which is attribute to the strong quenching of excited CO_2^* by H_2 and H_2O molecules as discussed above.

Fig. 5 presents images of the flame (Flame A) established at different strain rates. For the range of strain rates ($a_s = 15$–$143\ s^{-1}$) investigated, stable intense blue flames were observed. With the increase in a_s, the velocities of both the fuel and oxidizer streams increase. Consequently, the flame moves towards the oxidizer nozzle. For the range of strain rates investigated, the peak flame temperature decreases with increasing a_s due to the reduced residence time. At low strain rates it was difficult to establish a flat flame due to the buoyancy and pronounced suction effect. Higher values of strain rates ($a_s \geqslant 143\ s^{-1}$) were beyond the limit of the used mass flow controllers. At higher strain rates another flame in the background was observed as some fuel escaped. Slight orange glow is observed upstream of the flame location at high strain rates. The nature of this glow requires further experimental studies. The light emissions in the corresponding spectral range are typically not observed in CO flames. The several existing observations of the glow in this region were attributed to small $Fe(CO)_5$ impurities [35]. Iron pentacarbonil is readily formed in steel cylinders and supply lines containing carbon monoxide. However, the aluminum cylinder and plastic supply lines were used in the current experiments.

5.3. Effect of pressure, strain rate and equivalence ratio on syngas/air PPF structure

For preliminary analysis of partially premixed flames, digital images (cf. Fig. 6) of several PPFs were taken for different values of strain rates and partial premixing. At $a_s = 35\ s^{-1}$, $\phi = 6$ (cf. Fig. 6a) a typical double flame structure is observed with a weak rich premixed reaction zone (RPZ) established very close to the fuel nozzle and a non-premixed zone (NPZ) established near the stagnation plane and characterized by the blue flame due to CO oxidation in the NPZ. As ϕ increases the RPZ moves away from the fuel nozzle. At $a_s = 35\ s^{-1}$ and $\phi = 16$ (cf. Fig. 7) the RPZ and NPZ are very close to each other. For $a_s = 50\ s^{-1}$ similar trends are observed. With increase in a_s, the location of the RPZ is expected to move away from the fuel nozzle; however, the change in strain rate is too small to be distinguished. In Fig. 6c a yellowish orange flame is observed near the nozzle edge. A system of stainless steel screens is mounted ~3 mm deep in the nozzle duct to provide the uniform distribution of the gas flow. With reduction of the equivalence ratio, partially premixed flame travels upstream until it is stabilized on the top metal screen. The characteristic orange glow is observed in this

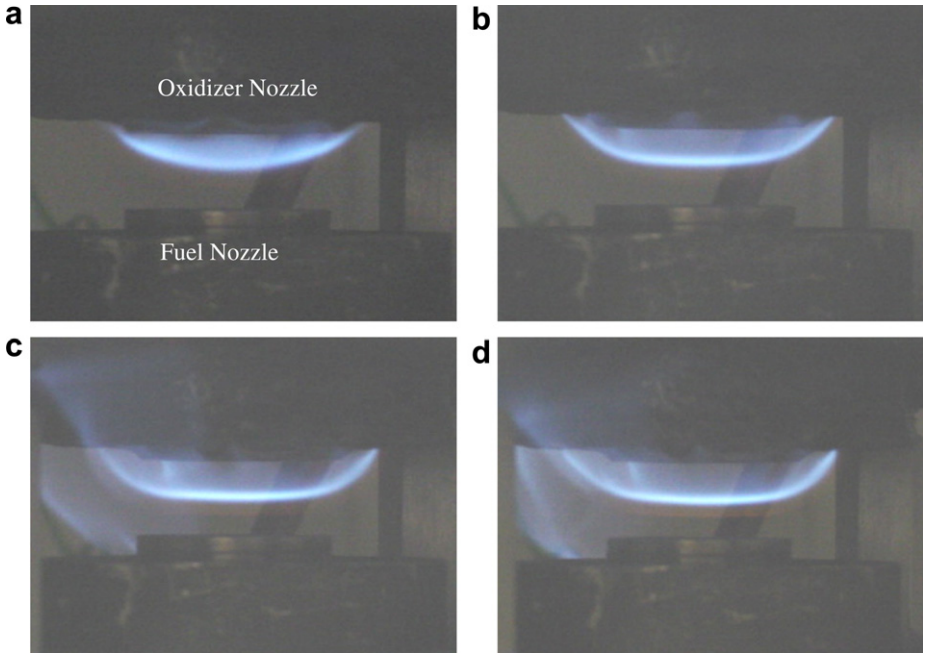

Fig. 5. Images of syngas/air non-premixed Flame A established at $p = 1$ atm for strain rates: 15 (a), 65 (b), 115 (c) and 143 s^{-1} (d).

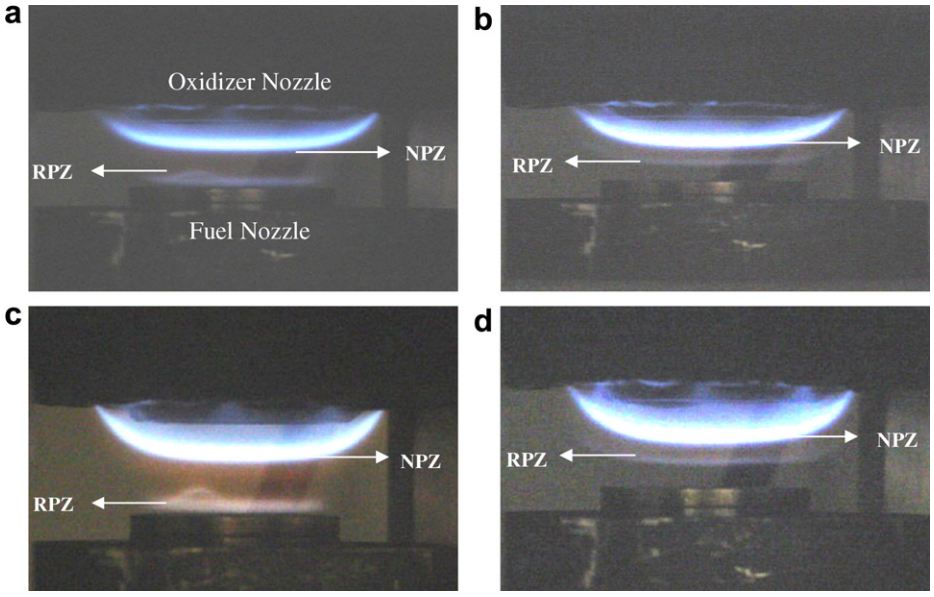

Fig. 6. Images of syngas/air PPFs established at $a_s = 35\ s^{-1}$, $\phi = 6$ (a) $a_s = 35\ s^{-1}$, $\phi = 16$ (b) $a_s = 50\ s^{-1}$, $\phi = 6$ (c) and $a_s = 50\ s^{-1}$, $\phi = 14$ (d) for Flame A.

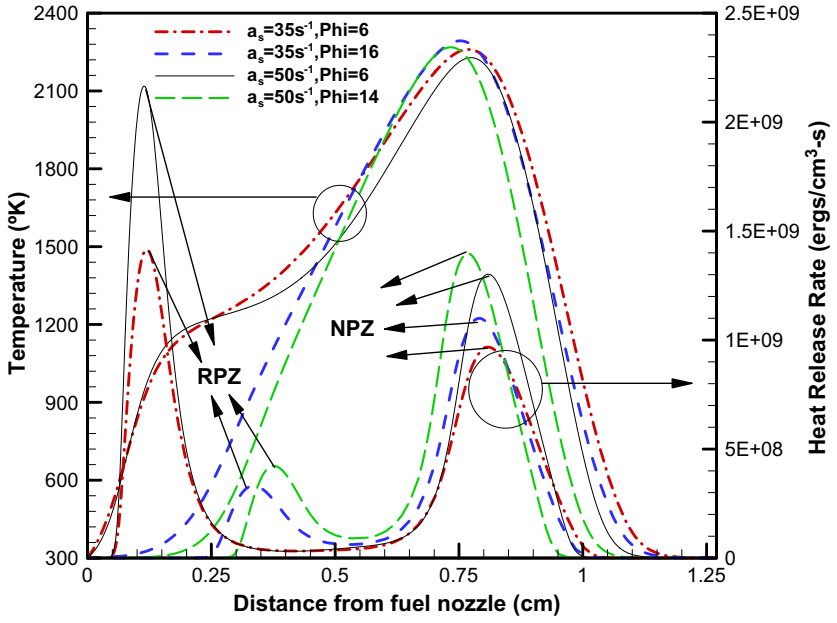

Fig. 7. Temperature profiles and heat release rates for syngas/air PPFs established at different strain rates and equivalence ratios for Flame A.

case due to the flame interaction with the screen material. This glow is generated by heated screen wires and strong radiating iron atoms transferred to the gas phase.

The above flames were also simulated numerically using the modified Davis et al. mechanism. Fig. 7 presents the temperature and heat release rate profiles for these flames. At $\phi = 6.0$, the flame structure is characterized by two spatially separated reaction zones namely, RPZ and NPZ, located by the two temperature and heat release rate peaks. The RPZ is very close to the fuel nozzle which is in agreement with the digital images presented in Fig. 6. The lower strain rate flame ($35\ s^{-1}$) predicts slightly higher temperatures owing to higher residence time. At higher ϕ values ($\phi = 16.0$), the temperature peaks appear to indicate a nearly merged flame structure. However, heat release rate profiles indicate two distinct peaks close to each other which is again consistent with the digital images in Fig. 6. The strain rates employed in experiments were relatively low. Since combustion in many practical systems involve small residence times and high pressures, it is of interest to study the syngas flame structure and NO_x characteristics at high strain rates and elevated pressures.

Fig. 8 presents temperature profiles computed using the modified Davis et al. mechanism for Flames *A* and *B* estab-

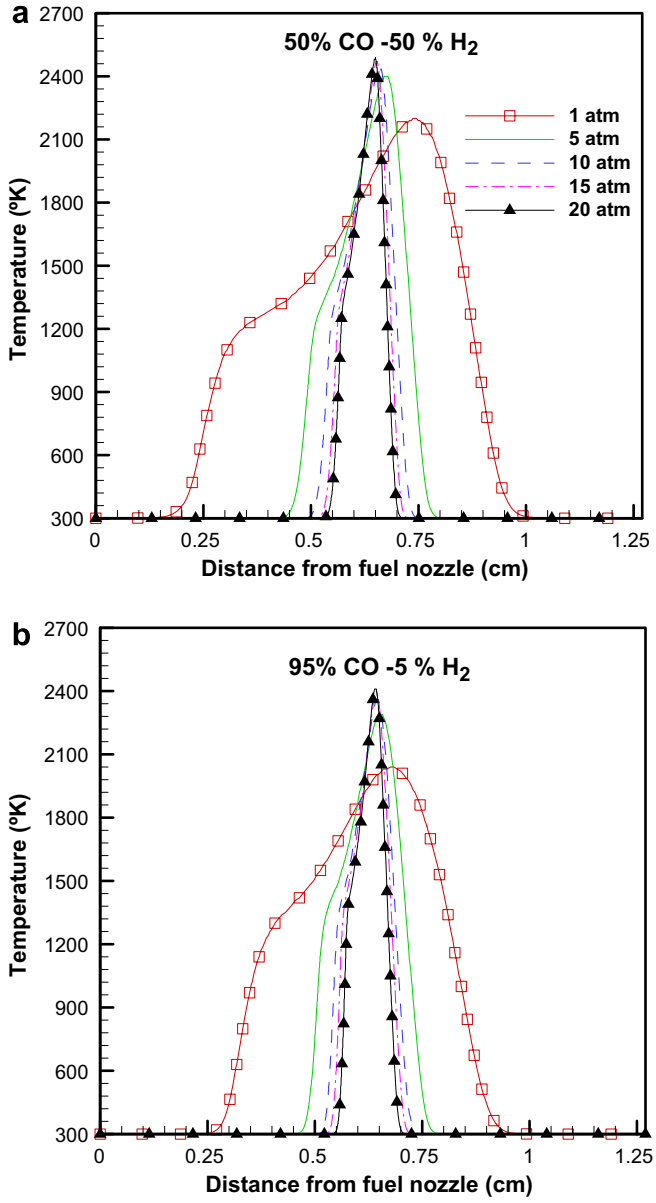

Fig. 8. Temperature profiles at different pressures for syngas/air PPFs (Flames A and B) established at $\phi = 6.0$, $a_s = 100\ s^{-1}$ and computed using the Davis mechanism.

lished at $a_s = 100\ s^{-1}$, $\phi = 6.0$, and different pressures. Based on the temperature profiles, the flame structures for Flames A and B are similar, except that the peak temperatures are higher for Flame A, since it has larger amount of H_2 than Flame B. In addition, Flame A is broader than Flame B, which can be attributed to the difference in unstretched laminar flame speeds for the two flames. The unstretched laminar flame speed for Flame A is higher compared to that for Flame B (cf. Fig. 9), and, therefore, the RPZ is stabilized more upstream, which increases the distance between the two reaction zones for Flame A.

As discussed earlier, the PPF structure is characterized by the presence of two reaction zones, namely a RPZ on the fuel side and a NPZ on the air side. As expected, the

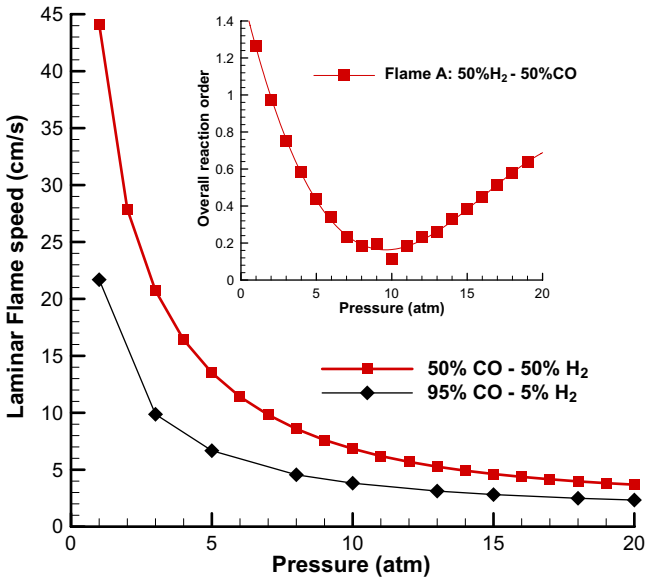

Fig. 9. Laminar flame speeds of Flames A and B plotted versus pressure at $\phi = 5.5$. Inset plots the overall reaction order as a function of pressure for Flame A.

thickness of both the reaction zones decreases with increasing pressure [23,28]. In addition, as pressure increases, the separation distance between the two reaction zones decreases, which can be attributed to the effect of pressure on the laminar burning velocity associated with RPZ. The flame speed associated with RPZ decreases with increasing p, and, consequently, this zone moves downstream to a location where the axial flow velocity matches the stretched laminar flame speed. The peak temperatures in RPZ are essentially invariant to pressure changes. This is expected as for the corresponding freely propagating flame simulated at $\phi = 5.5$ (not shown) the peak flame temperature with increasing pressure does not change appreciably. The NPZ moves upstream with increasing pressure which is due to the effect of pressure on mass diffusivity of species. At higher pressures the mass diffusivity is lower which causes the oxidizer to move towards the stagnation plane in search of fuel, and hence the NPZ moves upstream. The peak flame temperature at the NPZ increases appreciably with increase in pressure upto $p = 10$ atm. Above $p = 10$ atm, the increase in temperature with pressure is not as significant and the peak temperature values tend to level off with pressure. In addition, the temperature increases monotonically from RPZ to NPZ for syngas/air PPFs. However, for methane/air PPFs it was seen that there are regions of endothermicity in between the reaction zones [23,28] at high pressures ($p \geqslant 11$ atm). At $p =$ 20 atm, the temperature profiles exhibit a nearly merged flame structure. However, the heat release rate profile (not shown) still indicated two distinct peaks.

In order to further analyze the effect of pressure on the location of the RPZ, we simulated the corresponding freely propagating premixed syngas flames at different pressures. Fig. 9 plots the unstretched laminar flame speed against

pressure for Flames A and B, at $\phi = 5.5$. This equivalence ratio is near the rich flammability limit for both Flames A and B (cf. Fig. 3a), and, therefore, the premixed flame structure may be expected to mimic the RPZ structure of the PPF at $\phi = 6.0$. For pressure up to 10 atm, the unstretched laminar flame speed (S_u^0) decreases rapidly with increasing pressure, and thereafter exhibits a weak dependence on pressure. This trend is seen for both Flames A and B. S_u^0 as a function of p can be expressed as $S_u^0 = p^{(n/2)-1}$ [36], where (n) is the overall reaction order and computed from: $n = 2 + 2\left(\frac{\partial \ln(S_u^0)}{\partial \ln(p)}\right)$. The stretched and unstretched laminar burning velocities are related as: $S_u = S_u^0 - LK$ [37] where S_u denotes the stretched laminar burning velocity, L the Markstein length, and K the flame stretch. In the limit of small stretch, this equation is simplified to $S_u = S_u^0(1 - Ma_\infty Ka_\infty)$ [38] where Ka_∞ denoted the Karlovitz number representing the flame stretch and Ma_∞ the Markstein number representing both the sensitivity of laminar flame speed to stretch and preferential diffusion instability. Hence, trends in unstretched laminar flame speed directly affect the stretched flame speed and subsequently affect the location of RPZ. The inset plots the overall reaction order against pressure for Flame A. The overall reaction order initially decreases with increase in pressure up to $p = 10$ atm. This is due to the relative dominance of chain termination reaction compared to branching reactions (discussed later (cf. Fig. 10)) in this pressure range. This decrease in overall reaction order also leads to the rapid decrease in laminar flame speeds. Further increase in pressure causes the overall reaction order to increase due to the relative dominance of chain branching reactions compared to terminating reactions.

Sensitivity analysis was performed to identify the dominant reactions for Flames *A* and *B* at $\phi = 5.5$. Fig. 10 plots the sensitivity coefficients defined with respect to mass burning rate, indicating the sensitivity of the mass burning rate to various reactions. Hence, a reaction not appearing in this plot may not be important for mass burning rate calculations. Sensitivity coefficient (S_i) for ith elementary reaction is defined as $S_i = \frac{\partial\{\ln(m_b)\}}{\partial\{\ln(k_i)\}}$, where k_i is the reaction rate of ith elementary reaction and m_b is the mass burning rate. The common points observed for Flames A and B are as follows:

(1) In general, it is observed that mass burning rate is more sensitive to H_2 oxidation rather than CO oxidation chemistry.
(2) The sensitivity of chain branching reactions $H + O_2 \rightarrow O + OH$ and $HO_2 + H \rightarrow 2OH$ initially increases with increase in pressure up to $p = 5$ atm and decreases thereafter.

As expected, $CO + OH \rightarrow CO_2 + H$ is found to be the major CO oxidation reaction for Flame A. However, the mass burning rate is found to be sensitive to this reaction for Flame A only. This is due to the absence of OH radicals for Flame B owing to low concentrations of H_2(5%) in fuel mixture. Also, sensitivity of this reaction increases with increase in pressure for Flame A. The magnitude of sensitivity coefficient (for Flame A) of the chain terminating reaction $H + O_2(+M) \rightarrow HO_2(+M)$ initially increases with pressure and then decreases. At $p = 20$ atm, the mass burning rate is not sensitive to this reaction, and hence, the branching reactions relatively dominate causing the increase in overall reaction order. A validation of our sensitivity data are provided by the fact that sensitivity coefficients obtained using the Davis et al. mechanism for $\phi = 2.0$ and $\phi = 5.5$, 95%CO–5%H_2 mixture at $p = 1$ atm were in good agreement with the sensitivity data reported by McLean et al. [25]. Having examined the behavior of the RPZ, we now analyze the PPF structure in greater detail.

Fig. 11 presents the mole fraction profiles of the fuel constituents, i.e., H_2 and CO, at different pressures for Flame A. Typically in hydrocarbon (such as methane) PPFs, CO and H_2 are produced in the RPZ, and then transported to and consumed in the NPZ [22,23,28]. The H_2 mole fraction profiles in Fig. 11a indicate that H_2 is partially consumed in the RPZ with the remaining being consumed in the NPZ mainly through reaction: $OH + H_2 \rightarrow H + H_2O$. The first trough locates the RPZ, while the second trough locates the NPZ. Consequently, the distance between the two H_2 consumption troughs corresponds to the distance between the reaction zones, which decreases with pressure as discussed earlier. It is also important to note that the RPZ is characterized by the H_2 oxidation chemistry rather than CO oxidation chemistry, while the NPZ is characterized by both the H_2 and CO oxidation chemistries. The dominant reactions in the RPZ in order of importance are:

- $OH + H_2 \rightarrow H + H_2O$
- $H + O_2 + M \rightarrow HO_2 + M$
- $HO_2 + H \rightarrow 2OH$
- $H + O_2 \rightarrow O + OH$
- $O + H_2 \rightarrow H + OH$
- $CO + OH \rightarrow CO_2 + H$

The NPZ is characterized by the following dominant reactions in order of importance:

- $OH + H_2 \rightarrow H + H_2O$
- $H + O_2 \rightarrow O + OH$
- $O + H_2 \rightarrow H + OH$
- $CO + OH \rightarrow CO_2 + H$
- $H + OH + M \rightarrow H_2O + M$

In contrast to hydrocarbon PPFs where CO and H_2 are produced in the RPZ, for syngas/air PPFs, CO being a major fuel constituent is not produced in the RPZ, and is mostly consumed in the NPZ; the main CO consumption reaction being: $CO + OH \rightarrow CO_2 + H$ in both RPZ and NPZ. The CO peak and trough in Fig. 11b locate the RPZ and NPZ, respectively. Moreover, it seems that CO

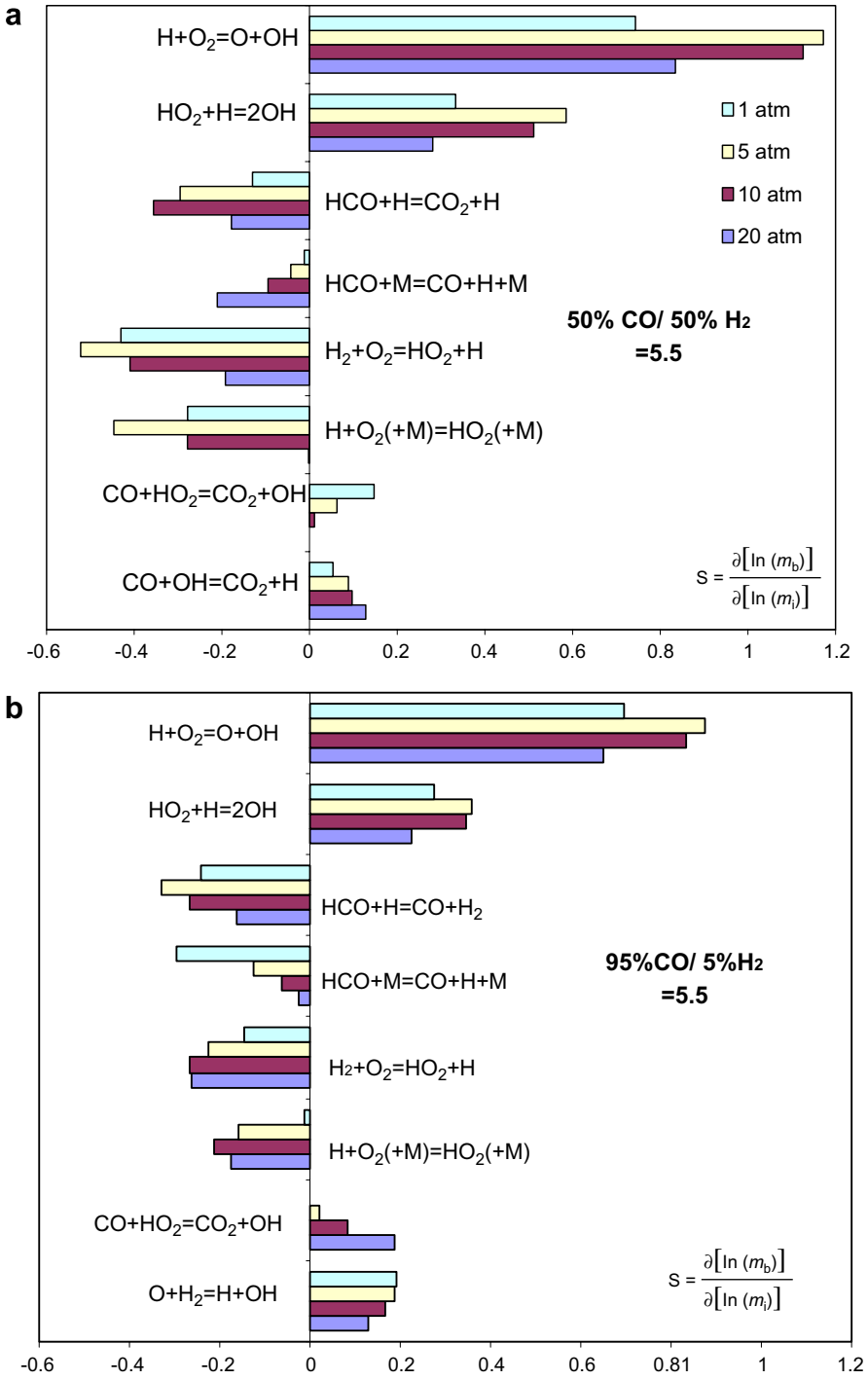

Fig. 10. Normalized sensitivity on mass burning rate for the most important reactions calculated at $\phi = 5.5$ for a premixed syngas/air mixture at different pressures for Flames A and B.

is being produced at the RPZ, which is not true as the local CO peak is due to the fact that H_2 diffuses faster than CO, which causes an increase in CO concentration locally at the RPZ. With increase in pressure the CO peak values shift towards the stagnation plane, which is in accordance with the downstream movement of the RPZ (cf. Fig. 8a) with pressure. Due to the nearly merged structure at high pressures the CO peak (at RPZ) seems to coincide with the CO consumption trough (at NPZ). CO consumption rate increases with increasing pressure which is the cause for higher peak temperatures at the NPZ (cf. Fig. 8a) and higher consumption gradients in Fig. 11b. It is also interesting to note that in contrast to our previous study dealing with high-pressure methane PPFs [23,28], there is no region of endothermicity and CO production between the two reaction zones for syngas PPFs.

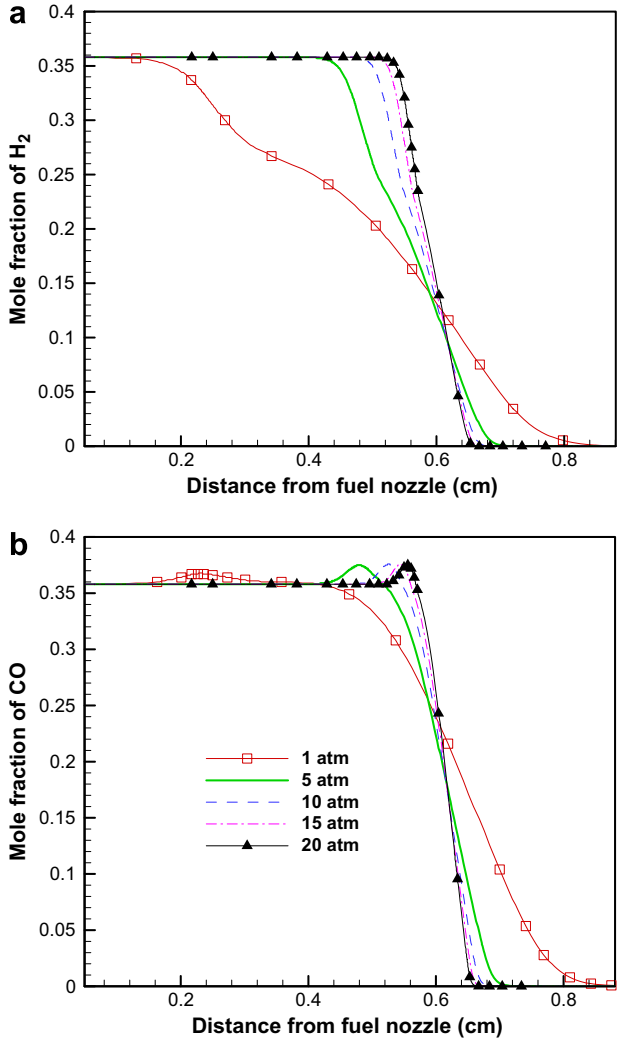

Fig. 11. Mole fraction profiles of H_2 (a) and CO (b) at different pressures for Flame A established at $\phi = 6.0$, $a_s = 100\ s^{-1}$ and computed using the Davis et al. mechanism.

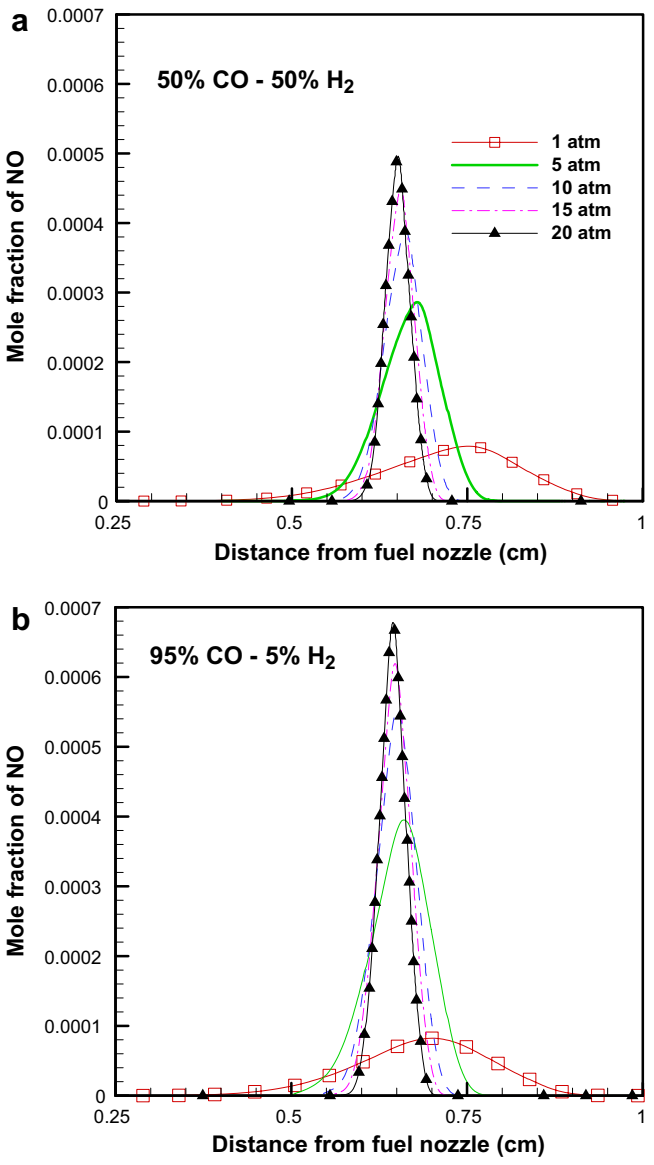

Fig. 12. NO mole fraction profiles for Flames A and B discussed in the context of Fig. 8.

5.4. NO_x emission characteristics of syngas PPFs

Fig. 12 presents the computed NO mole fraction profiles for Flames A and B, as discussed in the context of Figs. 8 and 11, at different pressures. Important observations are as follows:

(1) There is a single NO peak located in the NPZ at all pressures. The peak shifts towards the fuel nozzle and becomes closer to the stagnation plane, since the NPZ shifts towards the fuel nozzle with increase in pressure.
(2) For the conditions investigated, the contribution of NO_2 to total NO_x is found to be negligible.
(3) For the pressure range depicted in Fig. 12, most of NO production occurs through the thermal route, with the dominant reactions being R39: $N_2 + O \rightarrow NO + N$, R40: $N + O_2 \rightarrow NO + O$ and R41: $N + OH \rightarrow NO + H$.
(4) The peak NO mole fraction increases as the pressure is increased, since the flame temperature increases with pressure, implying that the NO production predominantly occurs through the thermal route. It is important to note, however, that the peak NO concentrations are higher for Flame B compared to those for Flame A. This is somewhat surprising, since both the flame temperature (cf. Fig. 8) and the rate of reaction R41 are higher (due to significantly higher OH concentration) for Flame A compared to those for Flame B. This can explained; however, by examining the NO reburn characteristics for these flames, as discussed later in this paper.

The global NO emission characteristics of syngas/air PPFs can be studied by plotting the NO emission index

as a function of pressure. The NO emission index is defined as

$$\mathrm{EINO} = \frac{\int_0^L M_{\mathrm{NO}}\dot{\omega}_{\mathrm{NO}}\,\mathrm{d}x}{-\int_0^L (M_{\mathrm{H_2}}\dot{\omega}_{\mathrm{H_2}} + M_{\mathrm{CO}}\dot{\omega}_{\mathrm{CO}})\mathrm{d}x}.$$

Here M represents the molecular weight, $\dot{\omega}$ the net production/consumption rate, L the distance between the nozzles, and x the axial coordinate. The emission index is a global parameter that has been commonly used to characterize NO emission from different flames. Fig. 13 presents the emission indices for total NO, as well as for NO produced through thermal, prompt, N_2O-intermediate, and NNH-intermediate mechanisms, plotted versus pressure for Flames A and B. The important observations are: (i) all the emission indices increase as pressure increases, (ii) most of NO is produced through the thermal route, (iii) prompt route is negligible as expected, due to the absence of CH_i species, (iv) reburn mechanism consumes NO, as indicated by the negative emission index for this mechanism, and (v) EINO first increases rapidly as pressure is increased, and then becomes nearly independent of pressure at higher pressures. It is also interesting to note that the peak NO concentration for Flame A is lower compared to that for Flame B (cf. Fig. 12), although the peak temperature is higher in Flame A (cf. Fig. 8). However, EINO of Flame A is higher than that of Flame B, which can be attributed to the fact that the NO production rate in Flame A is higher than that in Flame B.

The presence of reburn route in syngas flames is surprising since the initiating species for reburn mechanism in hydrocarbon flames are CH_i [33]. A rate of production analysis was performed, and it was observed that reactions R48: $NO + O + M \rightarrow NO_2 + M$, and R73: $NO + H + M \rightarrow HNO + M$ were the major consumers of NO. These reactions are not a part of the classical reburn mechanisms [33]. However, since these reactions consume NO in syngas flames, we have retained this terminology. Since, these two reactions are third body reactions, they become increasingly more important at higher pressures, as indicated in Fig. 13. The higher NO concentration in Flame B (compared to Flame A) in spite of its lower temperature, as noted in the preceding section (cf. Fig. 12), can also be attributed to the reburn mechanism. Due to a significantly higher concentration of H radicals in Flame A, the reburn mechanism consumes larger amount of NO, through reaction R73, in this flame compared to that in Flame B.

In order to further characterize the effect of syngas composition on NO emissions, we plot in Fig. 14a the peak NO mole fraction as a function of pressure for syngas PPFs established at $\phi = 6.0$, strain rate $= 100\ \mathrm{s}^{-1}$, and different syngas compositions namely, 98%CO–2%H_2 (Flame E), 95%CO–5%H_2 (Flame B), 85%CO–15%H_2 (Flame G), 75%CO–25%H_2 (Flame C), 50%CO–50%H_2 (Flame A), 25%CO–75%H_2 (Flame D) and 10%CO–90%H_2 (Flame F) by volume. Thermal NO was the dominant route for NO production for all these flames. For all seven flames,

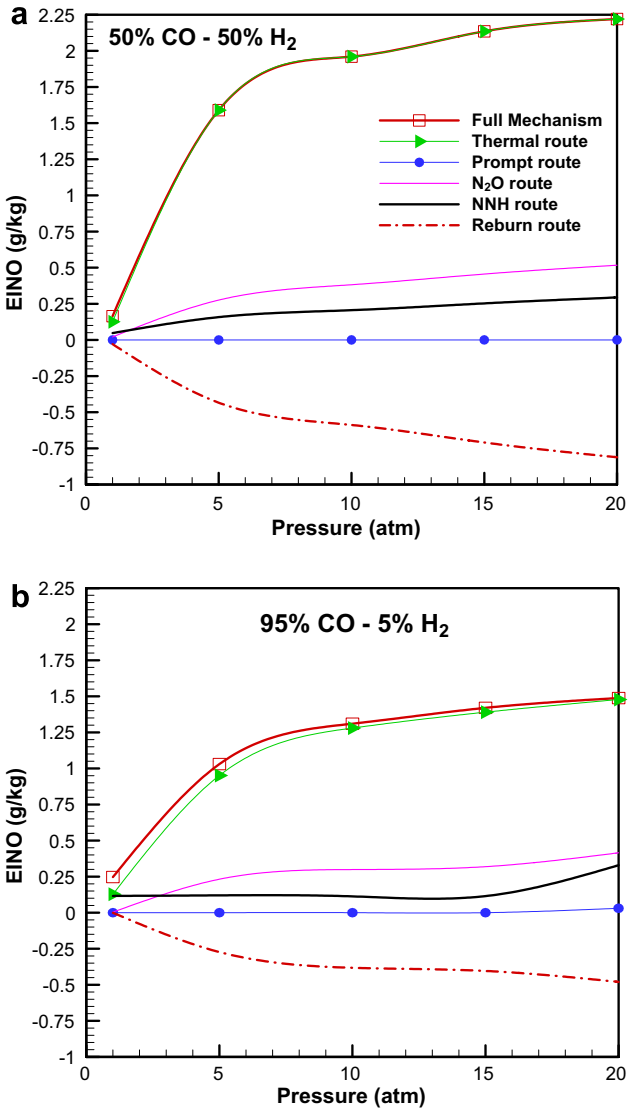

Fig. 13. Variation of emission indices of total, thermal, prompt, N_2O, NNH and reburn NO mechanisms with pressure for Flames A and B discussed in the context of Figs. 8 and 12.

the peak NO mole fraction increases rapidly with the increase in pressure upto $p = 10$ atm, implying that the thermal NO is the dominant NO production route, since the flame temperature also increases as the pressure is increased. Above $p = 10$ atm, the peak NO mole fraction seems to level off. This can be attributed to the fact the increase in flame temperature becomes less rapid (cf. Fig. 8), and the consumption of NO through the reburn route becomes increasingly important at high pressures.

Another important observation from Fig. 14a is that the peak NO mole fraction exhibits a non-monotonic variation with syngas composition. This non-monotonic behavior is presented more clearly in Fig. 14b. Results indicate that for any given pressure, there is an optimum syngas composition in terms of the CO mole fraction, for which the peak NO mole fraction has a minimum value. This CO mole fraction increases slightly from about 0.65–0.7, as the

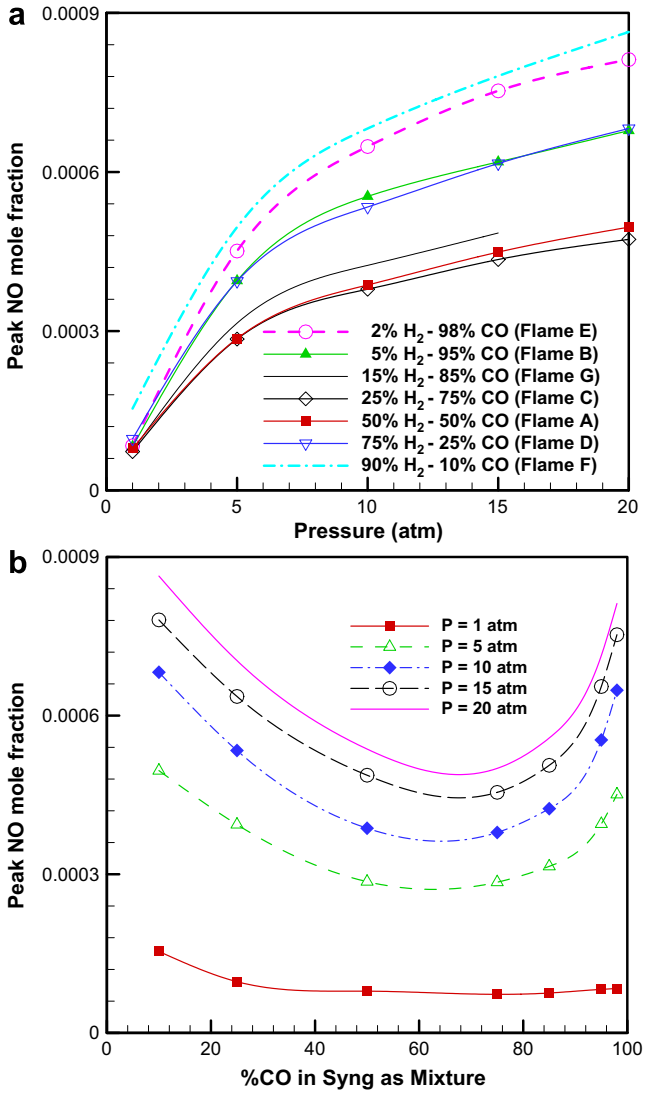

Fig. 14. Peak NO mole fraction, plotted versus pressure at different syngas compositions (a) and plotted versus % of CO in Syngas Mixture at different pressures (b) for partially premixed flames established $\phi = 6.0$, $a_s = 100\ s^{-1}$.

pressure is increased from 1 to 20 atm. The peak flame temperature for the above flames decreases in the following order: Flame F > Flame D > Flame A > Flame C > Flame G > Flame B > Flame E which is expected as the % of H_2 in the mixture increases from Flame E to Flame F. However, at a given pressure, as the amount of H_2 in syngas fuel is increased, the peak NO mole fraction first decreases (for H_2 between 0 and 25% by volume), and then increases (for $H_2 > 25\%$ by volume). This non-monotonic behavior can be attributed to the combined effects of thermal (through flame temperature) and reburn mechanisms, as the syngas composition is changed.

To explain this, we consider Flames B, C and D. Flame C has higher temperature but lower NO concentration than Flame B, since the NO consumption reaction (R73: $H + NO + M \rightarrow HNO + M$) is more pronounced, due to the higher concentration of atomic hydrogen, in Flame C. Therefore, the decrease in NO due to reburn route (reaction R73) is more pronounced than the increase in NO due to thermal route, as H_2 concentration in syngas is increased from 5% (Flame B) to 25% (Flame C). However, with further increase in H_2 concentration, the consumption of NO by reburn route levels off, and, consequently, the increase in NO due to thermal route becomes more pronounced, and the peak NO mole fraction is higher in Flame D compared to that in Flame C. Thus, an important observation from these results is the existence of an optimum syngas composition that yields the lowest amount of NO production in syngas PPFs, especially at high pressures. For the present results, this optimum composition corresponds to a syngas (H_2–CO mixture) containing between 65% and 70% CO by volume. This non-monotonic behavior was also observed at other equivalence ratios.

For the flames investigated, the peak flame temperatures were observed to range from 2000 to 2500 K. In this range, the thermal route is the dominant route for NO production which is expected. However, for state-of-art combustors operating ultra-lean and/or using diluents, the flame temperatures maybe lower than 1800 K. Under such conditions, other routes of NO production such as, N_2O-intermediate mechanism may become important. In future studies we intend to study the effect of diluents on syngas flames wherein, this low temperature NO routes may become critical.

6. Conclusions

In this paper, a numerical and experimental study of syngas non-premixed and PPFs at different pressures has been reported. The experimental investigation is performed to identify parametric regime, in terms of syngas composition and strain rate, for which counterflow syngas flames can be established under atmospheric conditions. Digital images of syngas non-premixed and PPFs established at different strain rates and syngas composition are presented for the first time. Three reaction mechanisms, namely the Davis et al., Mueller et al. and the GRI 3.0 mechanisms, have been evaluated using the available experimental data on laminar flame speeds and our measurements of non-premixed and partially premixed flames. Based on this evaluation, the Davis mechanism, in combination with a detailed NO_x mechanism, has been used to examine the structure and NO_x characteristics of syngas PPFs at high pressures. Important observations are:

1. Experiments indicate that stable syngas flames can be established in a counterflow configuration over a wide range of strain rates, syngas compositions, and equivalence ratios. For instance, it was possible to establish non-premixed flames using as little as ~0.5% H_2 by volume in CO–H_2 syngas mixtures.
2. Davis mechanism provides the most accurate prediction of the unstretched laminar flame speeds and non-premixed temperature profiles for flames under atmo-

spheric conditions. Consequently, this mechanism is used to examine the structure and NO_x characteristics of syngas PPFs at high pressures.

3. The syngas PPFs exhibit a typical double flame structure containing a RPZ on the fuel side and an NPZ on the oxidizer side. For the conditions investigated, the RPZ is characterized by H_2 oxidation, while the NPZ is characterized by both H_2 and CO oxidation. Unlike hydrocarbon PPFs, CO is not produced in the RPZ. However, similar to hydrocarbon PPFs, as the pressure is increased the thickness of each reaction zone and the distance between them decreases, while the flame temperature increases.
4. Results of sensitivity analysis indicate that the mass burning rate is more sensitive to H_2 chemistry rather than CO chemistry. Also, the primary CO oxidation reaction, $CO + OH \rightarrow CO_2 + H$, is important for only Flame A, which is due to the absence of key radicals like OH for Flame B, owing to low H_2 concentration (5%) in the fuel mixture.
5. For the syngas PPFs investigated, NO is produced predominantly through the thermal NO mechanism. However, a reburn route involving the consumption of NO, due to the third-body reactions $NO + O + M \rightarrow NO_2 + M$ and $H + NO + M \rightarrow HNO + M$, becomes increasingly important at high pressures.
6. As the pressure is increased or the amount of H_2 in syngas fuel is increased, the flame temperature increases monotonically. The amount of NO formed in syngas PPFs first increases rapidly with pressure, but then levels off at higher pressures. Moreover, at a given pressure, as the amount of CO in syngas fuel is increased, the peak NO mole fraction first decreases (for CO between 0% and 65% by volume) and then increases. This non-monotonic behavior can be attributed to the combined effects of thermal and re-burn mechanisms, as the syngas composition is changed. Thus, an important result from the present study pertains to the existence of an optimum syngas composition that yields the lowest amount of NO in syngas PPFs, especially at high pressures.

References

[1] Shilling NZ, Lee DT. IGCC – clean power generation alternative for solid fuels. GE Power Systems, Schenectady, 2003.

[2] Brdar RD, Jones RM. GE IGCC technology and experience with advanced gas turbines. GE Power Systems, GER-4207, Schenectady, 2000.

[3] Moore MJ. NO_x emission control in gas turbines for combined cycle gas turbine plant. Proc Inst Mech Eng 1997;211:43–52.

[4] Drake MC, Blint RJ. Thermal NO_x in stretched laminar opposed-flow diffusion flames with $CO/H_2/N_2$ fuel. Combust Flame 1989;76:151–67.

[5] Chung SH, Williams FA. Asymptotic structure and extinction of CO–H_2 diffusion flames with reduced kinetic mechanisms. Combust Flame 1990;82:389–410.

[6] Fotache CG, Tan Y, Sung CJ, Law CK. Ignition of $CO/H_2/N_2$ versus heated air in counterflow: experimental and modeling results. Combust Flame 2000;120:417–26.

[7] Rumminger MD, Linteris GT. Inhibition of premixed carbon monoxide–hydrogen–oxygen–nitrogen flames by iron pentacarbonyl. Combust Flame 2000;120:451–64.

[8] Jurgen JJL, Jim BWK, Sikke AK. Modeling and measurements of a 16-kW turbulent nonadiabatic syngas diffusion flame in a cooled cylindrical combustion chamber. Combust Flame 2001;125:1012–31.

[9] Giles DG, Som S, Aggarwal SK. NO_x emission characteristics of counterflow syngas diffusion flames with airstream dilution. Fuel 2006;85:1729–42.

[10] Charlston-Goch D, Chadwick BL, Morrison RJS, Campisi A, Thomsen DD, Laurendeau NM. Laser-induced fluorescence measurements and modeling of nitric oxide in premixed flames of $CO + H_2 + CH_4$ and air at high pressures: I. Nitrogen fixation. Combust Flame 2001;125:729–43.

[11] Natarajan J, Lieuwen T, Seitzman JM. Laminar speeds of synthetic gas fuel mixtures. Paper GT2005-68917. ASME-IGTI Turbo Expo, Reno, Nevada, June 6–9, 2005.

[12] Alavandi SK, Agrawal AK. Lean premixed combustion of carbon monoxide–hydrogen–methane fuel mixtures using porous inert media. Paper GT2005-68586. ASME Turbo Expo 2005. Reno, Nevada, June 6–9, 2005.

[13] Sung CJ, Huang Y, Eng JA. Effects of reformer gas addition on the laminar flame speeds and flammability limits of *n*-butane and *iso*-butane flames. Combust Flame 2001;126:1699–713.

[14] Huang Y, Sung CJ, Eng JA. Laminar flame speeds of primary reference fuels and reformer gas mixtures. Combust Flame 2004;139:239–51.

[15] Saxena P, Williams FA. Testing a small detailed chemical-kinetic mechanism for the combustion of hydrogen and carbon monoxide. Combust Flame 2006;145:316–23.

[16] Sun HY, Yang SI, Jomaas G, Law CK. High-pressure laminar flame speeds and kinetic modeling of carbon monoxide/hydrogen combustion. Proc combust Inst. 2007;31:439–46.

[17] Westbrook CK, Dryer FL. Chemical kinetics and modeling of combustion processes. Eighteenth international symposium on combustion. Pittsburgh: The Combustion Institute; 1981. pp. 749–67.

[18] Allen MT, Yetter RA, Dryer FA. High pressure studies of moist carbon monoxide/nitrous oxide kinetics. Combust Flame 1997;109:449–70.

[19] Davis SG, Joshi AV, Wang H, Egolfopoulos F. An optimized kinetic model of H_2/CO combustion. Proc Combust Inst 2005;30:1283–92.

[20] Mueller MA, Yetter RA, Dryer FL. Flow reactor studies and kinetic modeling of the $H_2/O_2/NO_x$ and $CO/H_2O/O_2/NO_x$ reactions. Int J Chem Kinetics 1999;31:705–24.

[21] Li J, Zhao Z, Kazakov A, Dryer FL. An updated comprehensive kinetic model of hydrogen combustion. Int J Chem Kinetics 2004;36:566–75.

[22] Xue HS, Aggarwal SK. Effects of reaction mechanisms on structure and extinction of partially premixed flames. AIAA J 2001;39:637–45.

[23] Som S, Aggarwal SK. A numerical investigation of methane air partially premixed flames at elevated pressures. Combust Sci Tech 2007;176(6):1085–112.

[24] Naik SV, Laurendeau NM. LIF measurements and chemical kinetic analysis of the Nitric Oxide formation in high pressure counterflow partially premixed and non premixed flames. Combust Sci Tech 2004;176:1809–53.

[25] McLean IC, Smith DB, Taylor SC. The use of carbon monoxide/hydrogen burning velocities to examine the rate of the $CO + OH$ reaction. Proc Combust Inst 1994;25:749–57.

[26] Puri IK, Seshadri K. Extinction of diffusion flames burning diluted methane and diluted propane in diluted air. Combust Flame 1986;65:137–50.

[27] Berta P, Aggarwal SK, Puri IK. An experimental and numerical investigation of *n*-heptane/air counterflow partially premixed flames and emission of NO_x and PAH species. Combust Flame 2006;145:740–64.

[28] Som S. A numerical investigation of methane air partially premixed flames at elevated pressures. M.S. Thesis, UIC, Oct' 05.
[29] Kee RJ, Grcar JF, Smooke MD, Miller JA, Meeks E. A Program for modeling steady, Laminar, One-dimensional premixed flames. Report SAND85-8240. Sandia National Laboratories, Livermore, CA, 1985.
[30] Kee RJ, Rupley FM, Miller JA. Chemkin ii: A fortran chemical kinetics package for the analysis of gas phase chemical kinetics. Technical Report SAND89-8009B, Sandia National Laboratories, 1993.
[31] Lutz AE, Kee RJ, Grear JF, Rupley FM. A Fortran program for computing opposed-flow diffusion flames. Sandia National Laboratories Report No. SAND96-8243, 1997.
[32] Smith GP, Golden DM, Frenklach M, Moriarty NW, Eiteneer B, Goldenberg M, et al. GRI Mech-3.0: <http://www.me.berkeley.edu/grimech/>.
[33] Miller JA, Bowman CT. Mechanism and modeling of nitrogen chemistry in combustion. Prog Energy Combust Sci 1989;15:287–338.
[34] Briones AM, Som S, Aggarwal SK. The Effect of Multi-Stage Combustion on NO_xEmissions in Methane-Air Flames. Submitted to Combust Flame 2006.
[35] Gaydon A. The spectroscopy of flames. 1st ed. Berlin: Springer; 1974.
[36] Egolfopoulos FN, Law CK. Chain mechanisms in the overall reaction orders in laminar flame propagation. Combust Flame 1990;80:7–16.
[37] Markstein GH. Non-steady flame propagation. New York: Pergamon; 1964. p. 22.
[38] Leis AP, Strechlow RA. On the propagation of turbulent flames. Combust Flame 1969;13:111–29.